



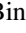
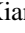





Stellar Atmospheric Parameters for Cool Dwarfs in Gaia Data Release 3

Cai-Xia Qu^{1,2} , A-Li Luo^{1,2} , Rui Wang^{1,2} , Hugh R. A. Jones³ , Bing Du^{1,2} , Xiang-Lei Chen^{1,2} , and You-Fen Wang^{1,2} 

¹ CAS Key Laboratory of Optical Astronomy, National Astronomical Observatories, Chinese Academy of Sciences, Beijing 100101, People's Republic of China; lal@nao.cas.cn

² School of Astronomy and Space Science, University of Chinese Academy of Sciences, Beijing 101408, People's Republic of China

³ School of Physics, Astronomy and Mathematics, University of Hertfordshire, College Lane, Hatfield, AL10 9AB, UK

Received 2022 October 28; revised 2023 August 16; accepted 2023 November 14; published 2024 February 1

Abstract

We provide a catalog of atmospheric parameters for 1,806,921 cool dwarfs from Gaia Data Release 3 (DR3) that lie within the range covered by LAMOST cool dwarf spectroscopic parameters: $3200 \text{ K} < T_{\text{eff}} < 4300 \text{ K}$, $-0.8 < [M/H] < 0.2 \text{ dex}$, and $4.5 < \log g < 5.5 \text{ dex}$. Our values are derived based on machine-learning models trained with multiband photometry corrected for dust. The photometric data comprise optical data from the Sloan Digital Sky Survey r , i , and z bands, near-infrared data from the Two Micron All Sky Survey J , H , and K bands, and mid-infrared data from the ALLWISE W1 and W2 bands. We used both random forest and light gradient boosting machine machine-learning models and found similar results from both, with an error dispersion of 68 K, 0.22 dex, and 0.05 dex for T_{eff} , $[M/H]$, and $\log g$, respectively. Assessment of the relative feature importance of different photometric colors indicated W1 – W2 as most sensitive to both T_{eff} and $\log g$, with $J – H$ being most sensitive to $[M/H]$. We find that our values show a good agreement with the Apache Point Observatory Galactic Evolution Experiment, but are significantly different to those provided as part of Gaia DR3.

Unified Astronomy Thesaurus concepts: Late-type dwarf stars (906); M dwarf stars (982)

1. Introduction

Cool dwarfs with low mass and low luminosity constitute more than 70% of the objects in the Galaxy. The determination of their stellar atmosphere parameters (APs) is vital for exploring the stellar formation, composition, and evolution history of the Galaxy (e.g., Bochanski et al. 2007). However, the estimation of the APs of cool dwarfs is difficult because of their complex atmosphere along with convective mixing. With ongoing improvements in atmosphere modeling for low-mass stars and advancements in the number of observations made and variety of instruments used, the measurement of the APs of cool stars has been carried out increasingly precisely.

Observations such as Jones et al. (1996) used the PHOENIX synthetic spectra to infer the APs of a few M dwarfs by comparing them with observed spectra. Casagrande et al. (2008) obtained the effective temperatures (T_{eff}) and bolometric luminosity of the M dwarfs based on the empirical relationship between the flux ratio in different bands and both the T_{eff} and the metallicity. Du et al. (2021) estimated the APs of M-type stars using an updated pipeline LASPM from low-resolution spectra, while Ding et al. (2022; hereafter, D22) applied the ULySS package with MILES interpolator model spectra to estimate the APs of M dwarfs. Furthermore, Li et al. (2021; hereafter, L21) published a stellar AP catalog of LAMOST M dwarfs using the SLAM machine-learning (ML) algorithm (Zhang et al. 2020).

The increasing availability of near-infrared spectra has also been utilized to determine precise APs of M dwarfs (e.g., Rojas-Ayala et al. 2010; Cristofari et al. 2022; Haqq-Misra et al. 2022). Rojas-Ayala et al. (2012) calibrated the H₂O–K2 index of K -band spectra of M dwarfs and estimated the T_{eff} and

$[M/H]$ of these objects based on NaI, CaI, and H₂O–K2 indexes.

Gaia is a satellite launched by the European Space Agency, with the goal of providing precise 3D maps and space motions of approximately one billion stars in our Galaxy (Gaia Collaboration et al. 2016a, 2016b; Cropper et al. 2018). In 2022, Gaia Data Release 3 (DR3) published complete data products (Gaia Collaboration et al. 2023), which include photometry in G , G_{BP} , and G_{RP} , objects with various types, and mean low-resolution (BP/RP) spectra and high-resolution Radial Velocity Spectrometer (RVS) spectra. With the BP/RP spectra, the APs of 470,759,263 sources within $G < 19 \text{ mag}$ were measured (Andrae et al. 2023), while with the RVS spectra, the APs of 5,591,594 objects were measured, most of which are AFGK stars (Recio-Blanco et al. 2023). Figure 1 shows diagrams with the distribution of the Gaia DR3 cool dwarfs. The left panel is the Hertzsprung–Russell (H–R) diagram of all Gaia DR3, color coded by number density. The objects below the blue dashed lines are considered to be cool dwarfs, whose Kiel diagrams ($\log g$ versus T_{eff}) obtained from BP/RP and RVS spectra are shown in the middle and right panels, respectively.

The AP distributions shown in the middle and right plots of Figure 1 are not consistent with each other. Nor are they consistent with the expectation of these dwarfs being objects largely on the main sequence and so approximately overlapping with standard isochrones. There are known problems with the external calibration of BP/RP spectra for cool objects that may impact the middle plot, e.g., Sarro et al. (2023). Given that cool dwarfs are relatively faint and in the narrow band of RVS spectra, we might anticipate the issues with the derivation of parameters in the right-hand plot that indicate the distinct selection of $\log g = 5.0$, as well as vertical features in the temperature selection that appear unphysical. We further cleaned the sample using quality flags (e.g. vbroad, vrad) and



Original content from this work may be used under the terms of the [Creative Commons Attribution 4.0 licence](https://creativecommons.org/licenses/by/4.0/). Any further distribution of this work must maintain attribution to the author(s) and the title of the work, journal citation and DOI.

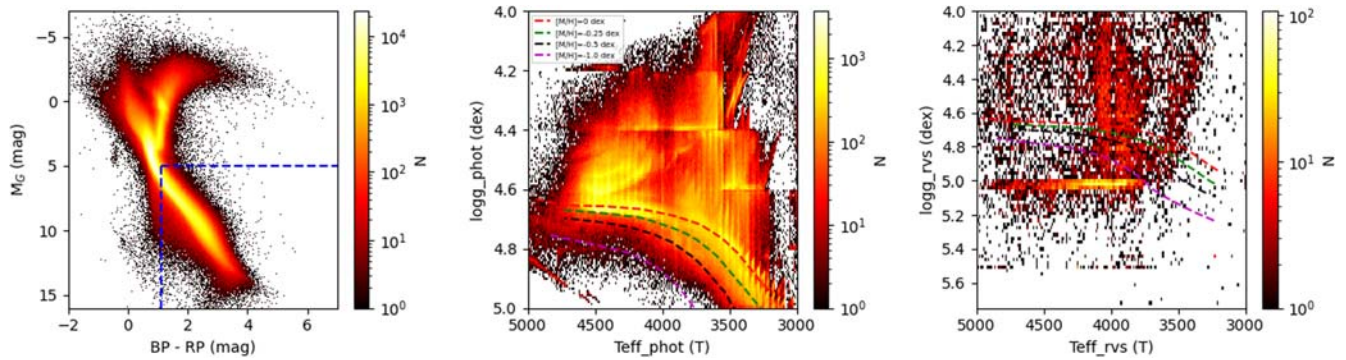


Figure 1. Distributions of Gaia objects and their APs. The left panel represents the H-R diagram of Gaia DR3 objects. The blue dashed lines provide preliminary bounds for our subsample of “cool dwarfs” based on the position of the vertical and horizontal blue lines at (1.3, 5). The middle panel plots the Kiel diagram (T_{eff} vs. $\log g$) based on parameters assigned using BP/RP spectra of the objects selected by the blue dashed lines in the left panel from Andrae et al. (2023), as well as PARSEC isochrones with an age of 6 Gyr and $[M/H]$ of 0, -0.25 , -0.5 , and -1.0 dex. The right panel depicts the same Kiel diagram for objects with parameters based on RVS spectra from Recio-Blanco et al. (2023), along with the same isochrones used in the middle panel.

made calibrations that were recommended by Recio-Blanco et al. (2023). However, there is a slight improvement because the remaining data points are too few to get a reliable statistical result. Thus, we guess that the RVS spectra are not sufficient in wavelength range to determine the APs for very cool dwarfs, which will hopefully be improved for the Gaia DR4. We also note the AP estimation using Gaia BP/RP spectra by Zhang et al. (2023), who develop a data-driven model to estimate the APs of 220 million objects in Gaia, though limited to $T_{\text{eff}} > 4000$ K.

High-resolution spectroscopy can provide precise stellar APs, but the number of objects that can be observed is limited. The high-resolution Sloan Digital Sky Survey (SDSS)/Apache Point Observatory Galactic Evolution Experiment (APOGEE) DR16⁴ published 22,991 cool dwarfs benefiting from infrared spectra that suffer less from line blending in the inferences of APs than optical spectra. However, an ongoing problem is the difference between the synthetic and observed spectra. Passegger et al. (2016) used new synthetic spectra based on the PHOENIX grid to determine APs from high-resolution spectroscopic observations. However, the $[\text{Fe}/\text{H}]$ reported from earlier estimations in some cases disagree with the new work by more than 3σ . The degeneracy of stellar APs is a significant issue. Rajpurohit et al. (2018) determined T_{eff} , $[\text{Fe}/\text{H}]$, and $\log g$ for 292 high-resolution spectra using the BT-Settl model, although the χ^2 map in Figure 3 of Rajpurohit et al. (2018) shows degeneracy between different parameter combinations.

On the other hand, low-resolution surveys can collect hundreds of thousands of cool dwarf spectra that should be representative of the larger sample of M dwarfs. LAMOST DR9⁵ has released a stellar AP catalog of M stars, comprising more than 0.6 million M dwarfs and benchmarked against other sources. Here we use these as the ground truth for ML to derive the APs of Gaia DR3 cool dwarfs with multiband photometry.

Multiband photometry provides a robust sampling of the spectral energy distribution to compensate for the lack of local information in spectra. Additionally, selection effects can be avoided when using multiband photometry. Compared to spectroscopy, multiband photometry can ensure the accuracy of AP estimation, although its precision may be relatively low. Furthermore, photometry can detect fainter objects and provide

a more consistent data distribution. In recent years, several ground- and space-based surveys have released a vast amount of photometry in the Milky Way, such as SDSS (York et al. 2000), Pan-STARRS (Kaiser et al. 2002), the Two Micron All Sky Survey (2MASS; Skrutskie et al. 2006), the Wide-field Infrared Survey Explorer (WISE; Wright et al. 2010), SkyMapper (Bessell et al. 2011), SAGA (Casagrande et al. 2014), Gaia (Gaia Collaboration et al. 2016a), SAGE (Zheng et al. 2018), and J-PLASS (Yang et al. 2022).

Taking advantage of multiband photometry and ML methods, we use optical and infrared photometry along with APs derived from LAMOST spectra to infer the stellar APs for cool dwarfs. Two different ML algorithms were used to train models for APs to ensure consistency and performance when testing and deriving parameters. The paper is organized as follows. Section 2 presents a detailed description of the cool dwarf sample, photometry surveys, and the data processes for the training sample. Section 3 describes the ML algorithms, model construction of APs, and feature importance analysis. Section 4 presents an AP catalog of cool dwarfs in Gaia DR3. Finally, the main conclusions are summarized in Section 5.

2. Data

In this section, we select cool dwarfs from Gaia DR3 to estimate their APs. Multiband photometry was used as input for our ML algorithms. The training sample was selected from LAMOST M dwarfs that had precise APs from two previous works.

2.1. Cool Dwarf Sample Selection

We select an appropriate sample of cool dwarfs from Gaia DR3 based on the dashed black lines in the color–magnitude diagram presented in Figure 2. Our rationale for this is based on finding simple but appropriate cuts indicated by the gray contours in the training sample. To construct these dashed black lines, we plot the LAMOST training sample presented in Section 2.4 as gray contours. First, we performed a linear fit on the training sample, indicated by the blue dashed line in Figure 2. Then this blue dashed line was shifted up and down by a magnitude to create two parallel black dashed lines enclosing the training sample. The magnitude limits for this training sample are set between $M_G = 7$ –11. These choices are based on noticing the change of the contour shape for M_G

⁴ <https://www.sdss.org/dr16/irspec/parameters/>

⁵ <http://www.lamost.org/dr9/v1.0/doc/ir-data-production-description>

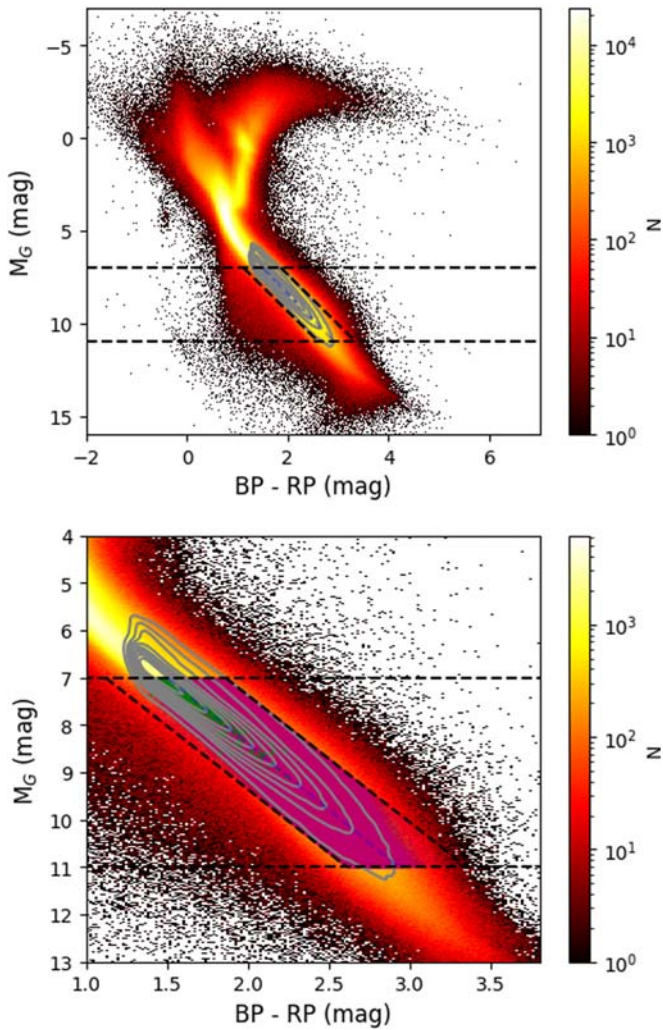


Figure 2. Color–magnitude diagram of Gaia stars and selected stars. Top: the background displays Gaia DR3 objects, while the training sample is plotted as gray contours with logarithmic scaling and fitted with a blue dashed line. The oblique black dashed lines are created by shifting the blue line up and down by 1.0 mag. The two horizontal black lines represent the absolute G magnitudes of 7 and 11 mag, respectively. Bottom: a zoom-in panel of the top panel with M_G between 4 and 13 mag with the addition of Gaia sources with APs. The green points are the sources with APs from RVS spectra, while the magenta points are the objects with APs from BP/RP spectra that lie within the black dashed selection box.

< 7 mag and that the last training set contour extends only slightly beyond $M_G = 11$. As shown in both panels of Figure 2, the box composed of black dashed lines is the selected region. We note that approximately 0.1 million sources with $BP - RP > 2.9$ mag lie beyond a significant density of training sample sources. For these objects, their APs will have an additional column labeled “flag” to caution others when utilizing these APs.

The bottom panel of Figure 2 shows a zoom-in for M_G between 4 and 13 mag, where the green and magenta objects are the Gaia sources with APs from RVS (587 sources) and BP/RP spectra (1,534,957 sources), respectively. Additionally, we used other criteria to exclude unreliable photometry and exclude unresolved binary stars. These criteria are as follows:

1. $G_{\text{mag}}/\text{error}_{G_{\text{mag}}} > 20$, $BP_{\text{mag}}/\text{error}_{BP_{\text{mag}}} > 20$, and $RP_{\text{mag}}/\text{error}_{RP_{\text{mag}}} > 20$;
2. Photometry error in each band less than 0.08 mag;

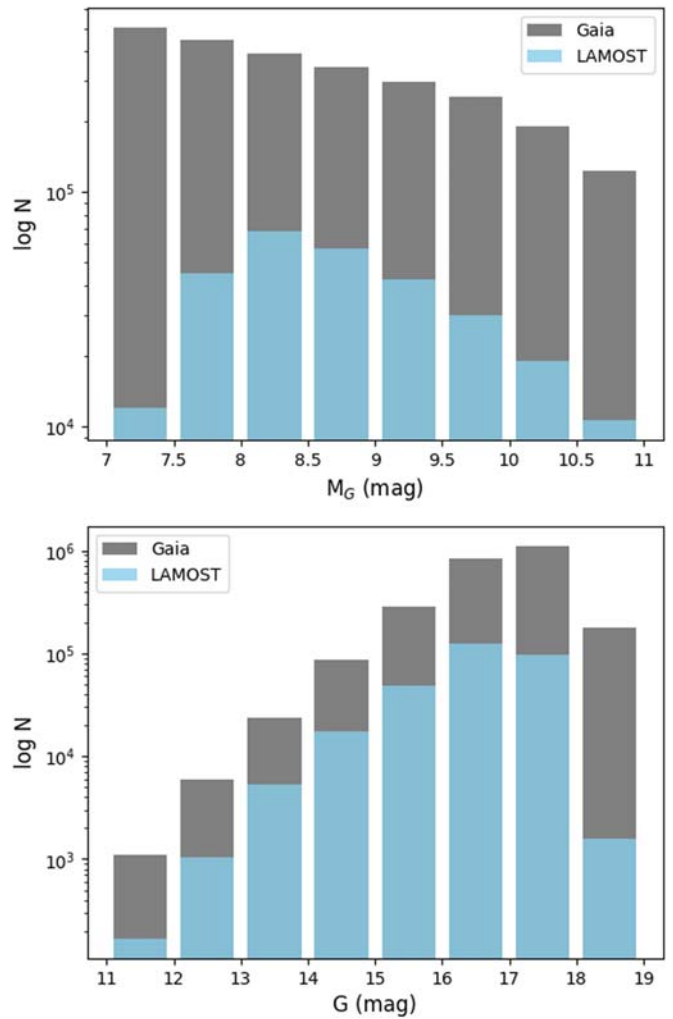


Figure 3. Source number comparison between Gaia cool dwarfs (in gray) and those with spectroscopic APs from LAMOST (in blue) for M_G (top) and G (bottom) photometry.

3. $RUWE < 1.4$; and
4. $\text{parallax}/\text{error}_{\text{parallax}} > 5$.

The basis for criterion 1 is to enable accurate photometry and astronomy (L21), as well as criteria 2 and 4 (Lin et al. 2022). Criterion 3 is for the avoidance of binary stars, which are likely to provide blended photometry (Gaia Collaboration et al. 2023), which also will be applied to the training sample.

We thus find 1,806,921 cool dwarfs from Gaia DR3 that overlap with the parameter space of our LAMOST training sample. Compared to spectroscopic data, only a small fraction of these stars already have APs from LAMOST. A comparison of the overlap between the Gaia cool dwarfs and LAMOST samples is shown in Figure 3.

2.2. Photometric Band Selection

To connect the APs of the LAMOST–Gaia matching cool dwarfs to those without LAMOST APs, we selected the multiband photometry from the optical to the infrared band as input data. SDSS is a 2.5 m telescope located at the Astronomical Observatory in Apache, New Mexico (York et al. 2000). There are five narrow bands u , g , r , i , and z (centered on 3551, 4686, 6166, 7480, and 8932 Å), ranging from the optical to the near-infrared wavelength range. However, many cooler dwarfs are too

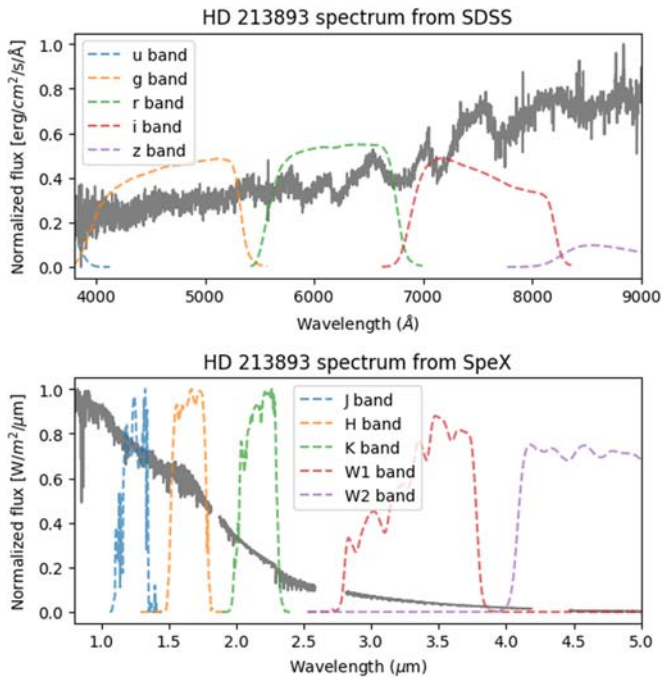


Figure 4. Example spectra of HD 213893 shown from 0.4 to 5 μm . The top panel shows an optical spectrum observed by SDSS, with RSR lines in the u , g , r , i , and z bands plotted. The bottom panel shows the infrared spectrum from SpeX, which covers the J , H , K , W1, and W2 bands.

faint to appear in the u and g bands, and so only the r , i , and z bands are considered. 2MASS is a near-infrared digital imaging survey of the entire sky conducted by the University of Massachusetts and IPAC at 1.25, 1.65, and 2.17 μm (Neugebauer & Leighton 1969). 2MASS can uniformly scan the entire sky in three near-infrared bands, J (1.25 μm), H (1.65 μm), and K (2.17 μm). WISE is an all-sky survey from 3 to 25 μm that aims to provide a vast repository of knowledge about the solar system, the Milky Way, and the Universe (Wright et al. 2010). It was launched on 2009 December 14 and updated the last data on 2013 March 21. The WISE source catalog contains the attributes of 563,921,584 resolved and point-like objects detected in the Atlas intensity images, with four bands W1, W2, W3, and W4 (3.4, 4.6, 12, and 22 μm). To ensure the quality of the photometry, we set the error of each band to less than 0.08 mag. We also exclude some possible extended sources with the flag 2MASS gal_contam and mp_glag = 0 and the flag ALLWISE ext_flag = 0 (Lin et al. 2022). We obtained a final Gaia cool dwarf sample of 1,806,921 objects by matching the multiband photometry in TOPCAT with a radius of 3". We do not include G , BP, and RP magnitudes as part of the training set in order to provide a solution that is independent. In particular, we avoid the use of BP and RP, since potentially they are part of the discrepancy presented in the middle plot of Figure 1.

The data features used for this work include photometry in eight bands (r , i , z , J , H , K , W1, and W2). As an example, we show the spectra of HD 213893, which is classified as M0 type and plotted in Figure 4 from optical to infrared. The top panel shows the optical spectra from SDSS, with relative system response (RSR) curves of five bands provided by SDSS.⁶ Prominent spectral features appear in the r , i , and z bands, such as the Na D line and molecular bands (CaH, TiO, and VO;

Lépine et al. 2003). The bottom panel presents the spectrum with a wavelength of 0.8–5.5 μm and a resolution of $R \approx 2000$, which is from the 3.0 m NASA Infrared Telescope Facility (Rayner et al. 2003). The corresponding RSR lines are presented according to the introductions to 2MASS⁷ and WISE.⁸ It can be seen that the flux density is high in the infrared range. Considering the accuracy in the W1 and W2 bands of WISE (Yuan et al. 2013), we adopted W1 and W2 photometry, although the spectral features are weaker in the far-infrared band. Therefore, photometry in the r , i , z , J , H , K , W1, and W2 bands was employed to represent the features of our data.

2.3. Extinction Correction

The 3D dust map method (Green 2018) consists of 2D maps (Planck Collaboration et al. 2014) and 3D maps (Green et al. 2018, 2015) applied to correct the extinction. In addition to the sky position of each point, reliable distance is also needed in the 3D dust map method. Here, we used the parallax from Gaia to compute the distance, which is considered to be useful to a distance of 4 kpc and contains all our objects. The extinction coefficients in different bands (Yuan et al. 2013; Casagrande et al. 2014; Casagrande & VandenBerg 2018a, 2018b; Lin et al. 2022) were used to transform to the corresponding bands. Furthermore, the absolute magnitudes in multiple bands were also computed.

2.4. Training Sample

To obtain AP labels of cool dwarfs, we used recent works of the AP estimation of LAMOST M dwarfs, crossmatching the two catalogs of L21 and D22. In the L21 catalog, the T_{eff} and $[\text{M}/\text{H}]$ are trained by APOGEE APs. Meanwhile the T_{eff} , $[\text{M}/\text{H}]$, and $\log g$ are all shown in the D22 catalog, trained by the ULySS package.

Figure 5 shows the comparison between the LAMOST training sample (D22) and the APOGEE sample (L21). The T_{eff} and $[\text{M}/\text{H}]$ of the training sample have good agreement with APOGEE, which is expected, because the parameters are obtained from models trained by the APOGEE data. The $\log g$ distribution has a scatter of 0.16 dex and bias of 0.01 dex. The $\log g$ is larger than 4.5. The AP distribution of our training sample is shown in the bottom panels of Figure 5. The distribution of T_{eff} is ranging from 3200 to 4300 K, with a peak at 4000 K. The $[\text{M}/\text{H}]$ is centered at -0.25 dex, ranging from -1 dex to 0.5 dex. Thus we find that there is no significant difference in the parameters determined by L21 and D22. Since the L21 T_{eff} and $[\text{M}/\text{H}]$ values are directly tied to the APOGEE scale, we adopt these and the $\log g$ values from D22. By selecting a signal-to-noise ratio (S/N) in the i band > 20 and 3σ clipping, we obtain a sample of 94,904 LAMOST objects with APs. These APs are the output labels of the models that will be trained.

3. Model Construction

To estimate the APs of Gaia cool dwarfs, we trained two ML models (random forest, RF, and light gradient boosting machine, LGB) using photometry in eight bands (r , i , z , J , H , K , W1, and

⁶ <http://classic.sdss.org/dr7/instruments/imager/index.php>

⁷ https://irsa.ipac.caltech.edu/data/2MASS/docs/releases/allsky/doc/sec6_4a.html

⁸ <https://wise2.ipac.caltech.edu/docs/release/allsky/expsup/>

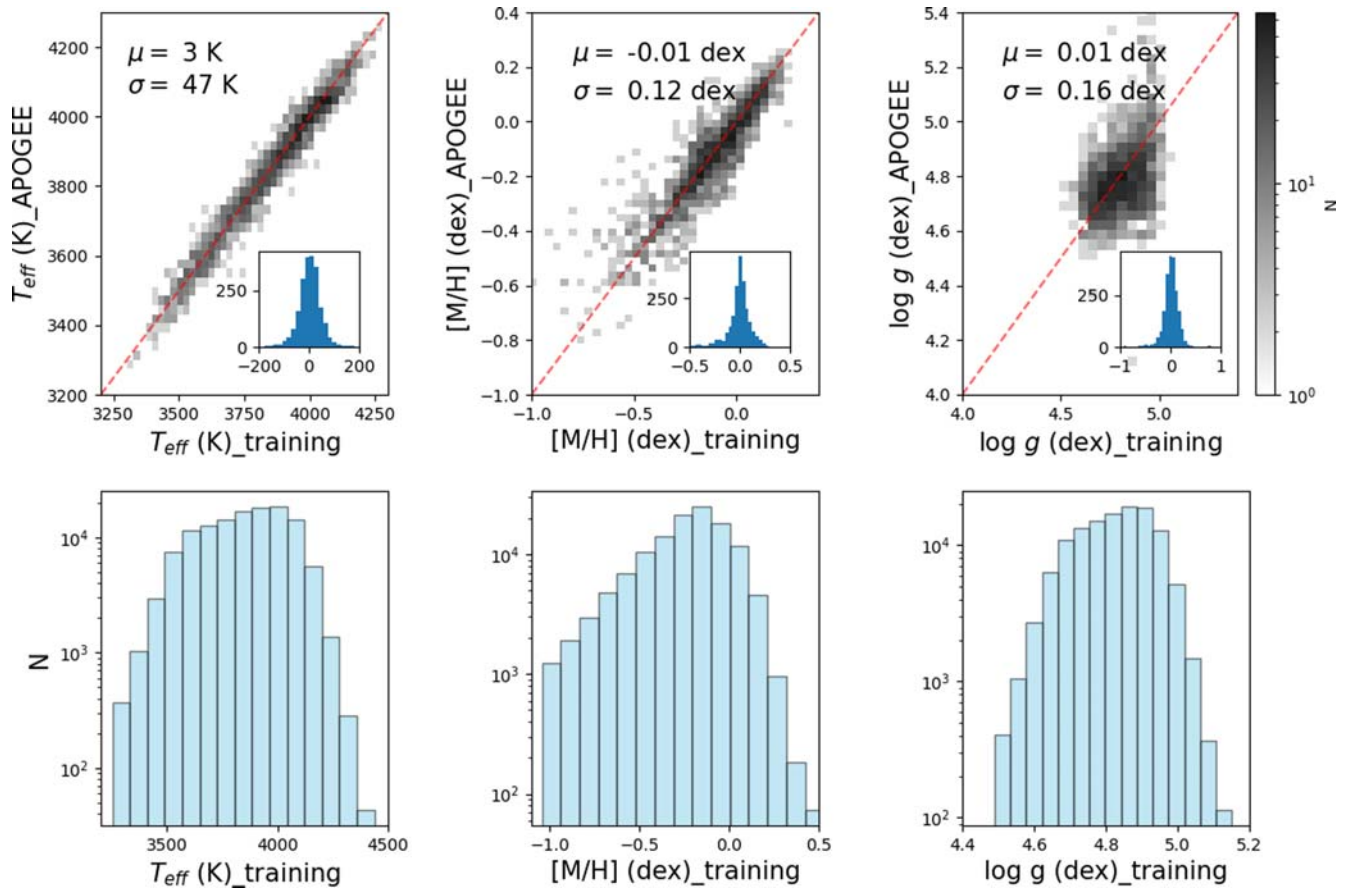


Figure 5. The upper row shows density plots comparing APs of the LAMOST training sample with those from APOGEE. The histograms inside each plot show the difference between the two samples. The bias (μ) and scatter (σ) are annotated inside each panel. The bottom row shows histogram distributions for the T_{eff} (left), $[M/H]$ (middle), and $\log g$ (right) of our training sample.

W2) and the APs of LAMOST/APOGEE M dwarfs (T_{eff} , $\log g$, and $[M/H]$). The feature contribution during model building was analyzed by the SHAP method.

3.1. Algorithms

As a part of the ML, the RF method integrates multiple decision trees to determine the result of the final vote of each tree (Breiman 1996a, 1996b). It runs efficiently on large databases and can handle thousands of input variables without deleting the variables. With the development of ML, RF has extensively worked in different fields as well as in astronomy for APs. For example, Bai et al. (2019) predicted the effective temperature for Gaia DR2 data by applying RF with an rms of 191 K.

In the gradient boosting family of ML models, LGB was proposed by the Microsoft DMTK team with a performance that exceeds other boosting decision tree tools (Ke et al. 2017). The histogram algorithm is applied to LGB, which occupies less memory and has a lower computational cost. Additionally, LGB uses a leafwise strategy to grow trees. The leaves with the largest split gain will be found and then split and looped. Compared to levelwise, leafwise can reduce more errors and get better accuracy when the number of splits is the same. However, overfitting will occur when the data size is small. Thus, there are several parameters in the algorithm to avoid overfitting in the training process, including the learning rate, `max_depth` (the defined depth of the tree), `num_leaves`

(leaf number in the tree), `lambda_l1` (L1 regularization term), and `lambda_l2` (L2 regularization term). A detailed description of LGB can be accessed at <https://lightgbm.readthedocs.io/en/latest/>. The LGB algorithm has been used in the detection of exoplanets (Malik et al. 2022), searches for cataclysmic variables (Hu et al. 2021), forecasts of solar flares (Ribeiro & Gradwohl 2021), as well as the prediction of stellar APs (Liang et al. 2022).

3.2. Feature Testing

In order to decide whether data features should use magnitudes or colors, the sample was divided into training and testing data, with fractions of 0.8 and 0.2, respectively. Table 1 lists the bias and scatter between the predicted and true APs of the testing data set for both RF and LGB. For the T_{eff} model, the σ of RF and LGB using colors is less than 70 K, which is better than that using magnitudes (see Table 1). The colors are more sensitive to T_{eff} , which is also actually known and has been applied to estimate the T_{eff} of different objects (Casagrande et al. 2021). Nonetheless, for the $[M/H]$ and $\log g$, the use of colors or magnitudes provides approximately the same scatter and bias. In order to be self-consistent with the T_{eff} , colors are also applied to be the features for the estimation of the $[M/H]$ and $\log g$ values. By comparing the performance of the test data, colors ($r - i$, $i - z$, $z - J$, $J - H$, $H - K$, $K - W1$, and $W1 - W2$) were adopted for use as the data features.

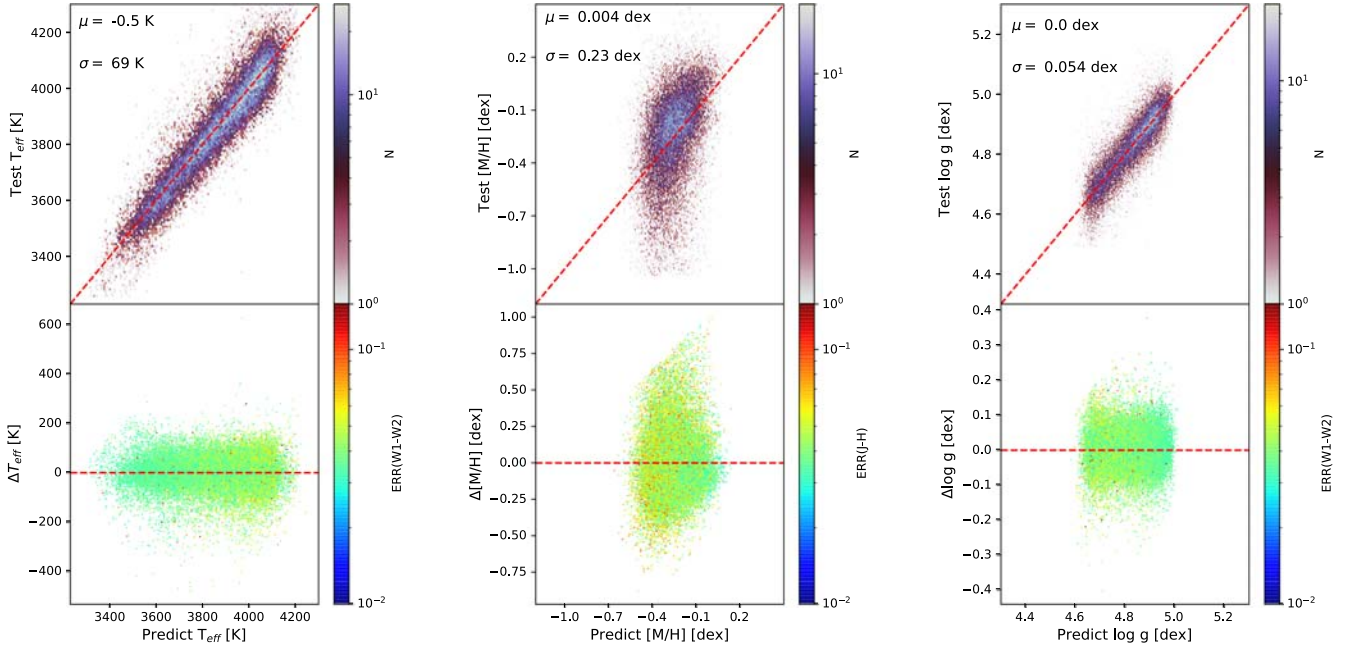


Figure 6. Comparison diagrams of the testing samples for the true and predicted values in terms of T_{eff} (left), $[M/H]$ (bottom), and $\log g$ (right). The top panels show the comparisons of the predicted values from RF and the true values, color coded by the number density of the test samples. The bottom panels indicate the difference between the predicted and true values, color coded by the photometric color error of $W1 - W2$ for T_{eff} and $\log g$ and color $J - H$ for $[M/H]$.

Table 1

Testing Results of the Two Methods Using Both Features of Magnitudes and Colors

	Feature = Magnitude			
	RF		LGB	
	μ	σ	μ	σ
T_{eff}	0.441	72	-5.14	80
$[M/H]$	-0.004	0.22	-0.006	0.23
$\log g$	-0.003	0.054	-0.003	0.057
	Feature = Color			
	RF		LGB	
	μ	σ	μ	σ
T_{eff}	-0.5	69	5.7	68
$[M/H]$	0.004	0.23	0.006	0.22
$\log g$	0.0	0.054	0.003	0.053

Note. Here, the magnitudes are absolute for extinction in the r , i , z , J , H , K , $W1$, and $W2$ bands, and the colors are $r - i$, $i - z$, $z - J$, $J - H$, $H - K$, $K - W1$, and $W1 - W2$. The μ and σ present the bias and scatter of the sample.

Using colors as features, Figure 6 shows the comparison of the predicted and true values of the testing data. The APs estimated by RF show a similar result to those with LGB. In the top panels, the predicted T_{eff} has a good agreement with that of the testing sample, having a bias of -0.5 K and a scatter of 69 K. The density distribution of $[M/H]$ has a slightly larger scatter of 0.2 dex. The $\log g$ distribution has a scatter of 0.05 dex without systematic bias. The residuals of the predicted and true values are shown in the bottom panels of Figure 6, with the photometric color error of $W1 - W2$ for T_{eff} and $\log g$ and color $J - H$ for $[M/H]$. The points with different photometric errors are randomly distributed around the residual

APs. Thus, the effect of the photometric error on estimating APs is not considered further.

3.3. Feature Importance Analysis

It is instructive to analyze the importance of features on the APs of cool dwarfs. We applied a Python package *shap* to compute the Shapley Additive exPlanations (SHAP) value of each feature (Lundberg & Lee 2017), which can create an explanation for the feature contribution to the model. The SHAP values of each feature are calculated and plotted in a SHAP summary graph. The vertical axis shows features ordered by their importance for modeling. The color is the feature value of the training sample. The horizontal axis indicates the SHAP value of each feature, which is positive and negative. The larger the absolute SHAP value of a feature, the larger the influence of this feature during model building.

We find similar results from both the RF and LGB methods, but here we only present the SHAP graph for RF in terms of T_{eff} , $[M/H]$, and $\log g$ in Figure 7. The top panel is the SHAP graph for the T_{eff} model, color coded by the feature values. The color $W1 - W2$ has the largest positive relationship to the SHAP value, which means $W1 - W2$ is the most sensitive to variations in T_{eff} . In the middle panel of the $[M/H]$ model, the near-infrared bands play a more important role during model building.

The three most important colors $J - H$, $W1 - W2$, and $H - K$ are all in the infrared bands, indicating that the infrared photometry is key to estimating the $[M/H]$. Schmidt et al. (2016) have also explored the colors $J - K$ and $W1 - W2$ as promising metallicity indicators for the T_{eff} and $\log g$ of the M dwarfs. In the $\log g$ SHAP graph, the color $W1 - W2$ is the most effective feature, followed by the $z - J$ and $J - H$. The three most important features for AP estimation are summarized in Table 2. It can be found that the near- and mid-infrared

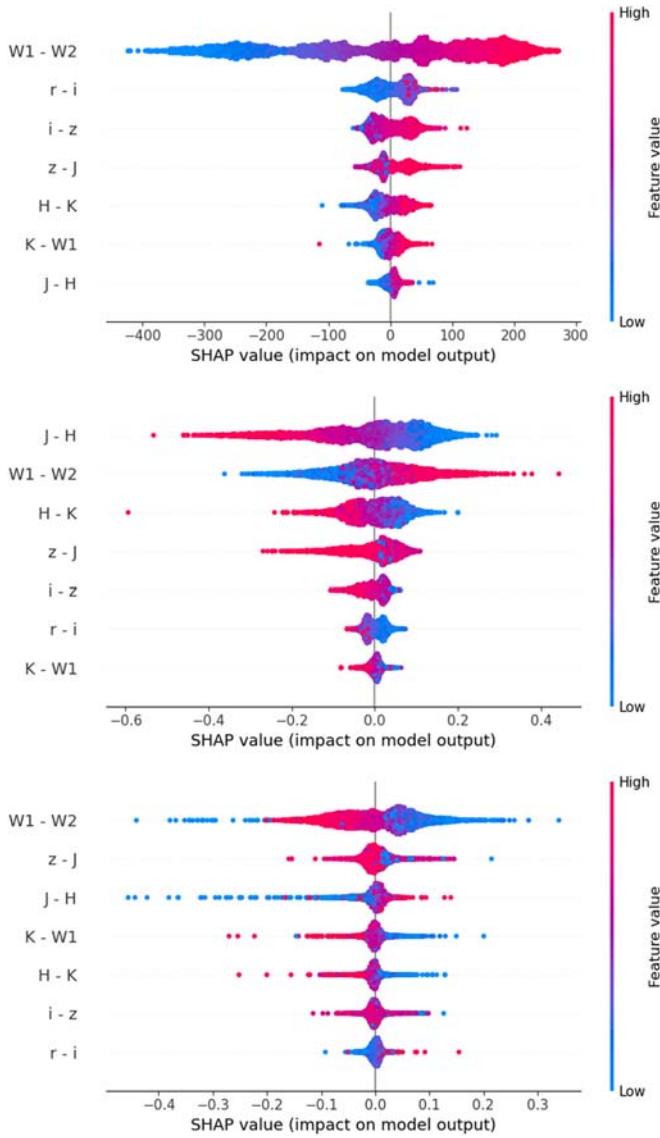


Figure 7. Feature importance graph during model building for T_{eff} (top), $[M/H]$ (middle), and $\log g$ (bottom). The color is the feature value, the x-axis is the SHAP value, and the y-axis for each feature is ordered by their contribution to model construction.

Table 2

The Three Most Important Features That Are Sensitive to T_{eff} , $[M/H]$, and $\log g$ during the Modeling Process

	T_{eff}	$[M/H]$	$\log g$
First	W1 - W2	J - H	W1 - W2
Second	r - i	W1 - W2	z - J
Third	i - z	H - K	J - H

photometry is more sensitive to the stellar AP variation. The importance of infrared photometry for M dwarfs has long been known—e.g., Glass (1975) introduced M dwarfs in JHK colors being quite distinct from M giants causing the dominating water opacity. Almendros-Abad et al. (2022) found that the H broad band is the most relevant feature for the estimation of the $\log g$ of M dwarfs using near-infrared spectroscopy. Thus, our finding of the significance of infrared photometry for the determination of APs for M dwarfs is in line with expectations.

Table 3

Observed and Derived Parameters for Our Catalog of Gaia Cool Dwarfs

Column	Unit	Description
source_id		Gaia DR3 source ID
RAdeg	deg	R.A.
DEdeg	deg	Decl.
Mrmag	mag	Absolute SDSS r -band magnitude (1)
Mimag	mag	Absolute SDSS i -band magnitude (1)
Mzmag	mag	Absolute SDSS z -band magnitude (1)
MJmag	mag	Absolute 2MASS J -band magnitude (1)
MHmag	mag	Absolute 2MASS H -band magnitude (1)
MKmag	mag	Absolute 2MASS K -band magnitude (1)
MW1mag	mag	Absolute ALLWISE W1-band magnitude (1)
MW2mag	mag	Absolute ALLWISE W2-band magnitude (1)
Teff-RF	K	Effective temperature from RF
e_Teff-RF	K	Uncertainty in T_{eff} -RF (2)
[M/H]-RF	dex	Metal abundance from RF
e_[M/H]-RF	dex	Uncertainty in $[M/H]$ -RF (2)
logg-RF	dex	Surface gravity from RF
e_logg-RF	dex	Uncertainty in $\log g$ -RF (2)
Teff-LGB	K	Effective temperature from LightGBM
e_Teff-LGB	K	Uncertainty in T_{eff} -LGB (2)
[M/H]-LGB	dex	Metal abundance from LGB
e_[M/H]-LGB	dex	Uncertainty in $[M/H]$ -LGB (2)
logg-LGB	dex	Surface gravity from LGB
e_logg-LGB	dex	Uncertainty in $\log g$ -LGB (2)
flag		boundary of BP - RP = 2.9 (3)

Note. (1) The photometry in each band is the absolute magnitude for reddening and extinction. (2) The uncertainties of the APs are the dispersion of 100 predicted values, from models trained by 100 randomly selected subtraining samples. (3) The flag is the boundary of BP - RP = 2.9 mag, flag = 1, while BP - RP > 2.9, otherwise flag = 0.

4. Parameterization for Gaia Cool Dwarfs

In this section, we estimate the APs of Gaia DR3 cool dwarfs using the trained RF and LGB models in Section 3. We provide a catalog of APs for 1,806,921 cool dwarfs in Gaia DR3. We compare our estimated APs to those provided by the Gaia DR3 release based on Gaia BP/RP spectra and RVs spectra.

4.1. AP Catalog from Photometry

In this section, we determine the APs for Gaia cool dwarfs using the models trained in Section 3. We provide a stellar AP catalog of 1,806,921 cool dwarfs, containing multiband photometry, T_{eff} , $[M/H]$, and $\log g$ by RF and LGB, and the corresponding uncertainties. Here, the uncertainty is derived from the multiple recalculations based on the Monte Carlo method. We trained 100 different models using randomly selected subtraining samples. Then the 100 APs for each object are predicted by repeated ML models applied to compute the dispersion as the uncertainty of this object. The field descriptors of the catalog are listed in Table 3 and an example section of the catalog is shown in Table 4. The complete catalog is accessible from China-VO at doi:10.12149/101330.

In the catalog, the uncertainties of our APs are provided to demonstrate the computed error. The density distribution of the uncertainties for T_{eff} , $[M/H]$, and $\log g$ as a function of the distance is shown in Figure 8. These stars are within 3 kpc and have uncertainties of T_{eff} , $[M/H]$, $\log g$ less than 65 K, 0.08 dex, and 0.05 dex, respectively. Objects with larger uncertainties are the later M spectra types, which is not

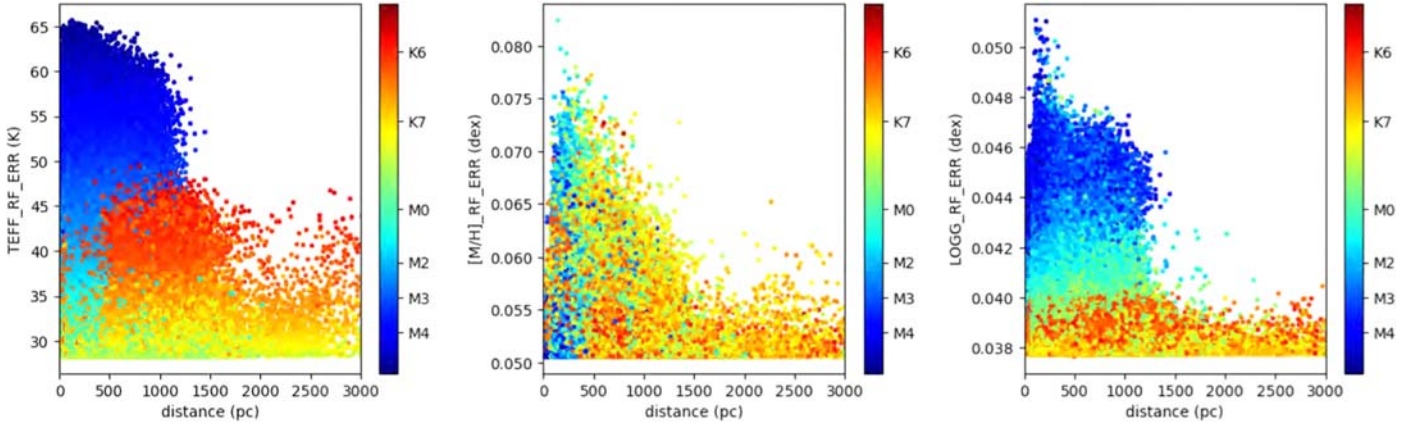


Figure 8. Density distribution of the uncertainties of T_{eff} (left), $[M/H]$ (middle), and $\log g$ (right), along with the distance, color coded by spectra type. Here, the error of the APs is the dispersion of 100 predicted values by repeating modeling using 100 subtraining samples.

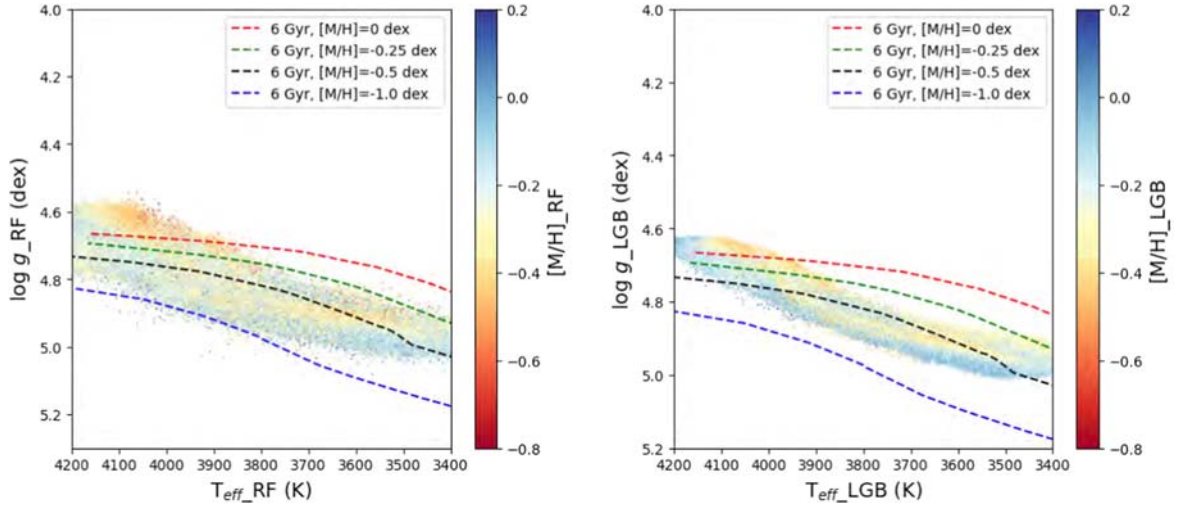


Figure 9. Kiel diagram of our catalog: $\log g$ as a function of T_{eff} color coded by $[M/H]$. The solid lines indicate PARSEC isochrones with an age of 6 Gyr and various $[M/H]$ s. The left panel shows the H-R diagram of our catalog predicted by RF, plotting four isochrones with the age of 6 Gyr and $[M/H]$ of 0, -0.25 , -0.5 , and -1.0 dex. The right panel indicates the H-R diagram of our catalog predicted by LGB, with the isochrones the same as in the left panel.

Table 4
The Stellar AP Catalog of Gaia Cool Dwarfs

Gaia DR3 SourceID	$T_{\text{eff}}\text{-RF}$	$[M/H]\text{-RF}$	$\log g\text{-RF}$	$T_{\text{eff}}\text{-LGB}$	$[M/H]\text{-LGB}$	$\log g\text{-LGB}$
352221678055936	3950	-0.12	4.80	3936	-0.23	4.80
354523780537216	3662	-0.34	4.92	3645	-0.40	4.91
357792251311232	3653	-0.14	4.93	3618	-0.18	4.93
360541030376576	4180	-0.29	4.67	4157	-0.26	4.64
361296944678016	3837	-0.01	4.81	3827	-0.02	4.84
363014931564416	4180	-0.36	4.64	4073	-0.35	4.66
363461608162048	3667	-0.4	4.91	3656	-0.38	4.91
363495967900032	3771	-0.32	4.87	3770	-0.32	4.86
363560391977856	3417	-0.12	4.99	3438	-0.13	4.96
367138100139136	3813	-0.29	4.86	3813	-0.23	4.84

Note. The complete table can be accessed from China-VO at doi:[10.12149/101330](https://doi.org/10.12149/101330).

surprising since this is where the training set is comparatively smaller.

Figure 9 presents the Kiel diagram of our catalog. We also show the PAdova and TRieste Stellar Evolution Code (PARSEC) theoretical tracks, at an age of 6 Gyr, and different

$[M/H]$ values from PARSEC version 1.2S (Bressan et al. 2012; Chen et al. 2015). The points in the left panel (predicted by RF) overlap with four isochrones with $[M/H] = 0, -0.25, -0.5,$ and -1.0 dex, and the same isochrones are in the right panel (predicted by LGB). It can be seen that the APs of LGB are less

scattered than those of RF. Nonetheless, the greater scatter of the LGB APs may actually be more physically realistic, given the expected scatter in the APs of the objects.

4.2. Parameter Comparisons

In this section, we compare our estimated APs with three catalogs, including APs from high- and low-resolution spectra of Gaia DR3, as well as APOGEE spectra.

4.2.1. Comparison with APs from APOGEE Spectra

APOGEE is one of the parts of SDSS. The stellar APs and metal abundances are determined by the APOGEE Stellar Parameters and Abundances Pipeline (ASPCAP), which analyzes the spectra of the APOGEE targets (Gunn et al. 2006; Holtzman et al. 2018). ASPCAP first obtains stellar parameters by fitting the entire spectrum; second, the individual element abundance is decided by fitting a limited spectrum associated with the element. ASPCAP is known to have the potential to allow eight parameters, including effective temperature T_{eff} , surface gravity $\log g$, etc. We crossmatched our sample with the APOGEE DR16 stellar AP catalog and selected cool dwarfs by following these criteria:

1. $ASPCAPFLAG = 0$ and $STARFLAG = 0$;
2. S/N of APOGEE > 30 ;
3. $T_{\text{eff_error}} < 150$ K, $\log g_{\text{error}} < 0.08$ dex, and $[M/H]_{\text{error}} < 0.02$ dex;
4. 3σ clipping for T_{eff} , $[M/H]$, and $\log g$; and
5. 3200 K $< T_{\text{eff}} < 4200$ K and $\log g > 4.5$ dex.

Figure 10 shows the predicted APs compared with APOGEE DR16. As both RF and LGB yield similar results, we only display the APs from RF for comparison with the APOGEE DR16 data. The T_{eff} distribution has a good agreement, with a bias of -3 K and a scatter of 55 K. This agreement was expected, since our training sample was labeled by APOGEE high-resolution spectra. The $[M/H]$ distribution has a bias of -0.03 dex and a scatter of 0.13 dex, while the $\log g$ estimation has a bias of 0.01 dex and a scatter of 0.11 dex. Overall, the APs of this work are in good agreement with APOGEE DR16.

4.2.2. Comparison with APs from BP/RP Spectra

We performed a crossmatch of Gaia DR3 APs from BP/RP spectra, APs with our catalog in TOPCAT, and excluded sources without APs. Additionally, we selected objects of $T_{\text{eff}} < 4300$ K, $\log g > 4$ dex, and $[M/H]$ from -1.0 to 0.1 dex to ensure a valid comparison. A total of 1,599,278 objects were included and are displayed in Figure 11. The yellow points represent RF APs from the multiband photometry in our work, while the gray points represent the results from BP/RP spectra of Gaia DR3. The gray points suggest a wide variety of artifacts in the Gaia DR3 APs that appear to be unphysical. In contrast, our work provides estimations for cool dwarfs that appear to be much more in line with those expected based on models, e.g., in Figure 9.

4.2.3. Comparison with APs from RVS Spectra

In addition to the APs from low-resolution BP/RP spectra, Gaia DR3 also provides the APs from high-resolution spectra. In this study, we select common objects between RVS and our catalog. After performing the matching process, we were left

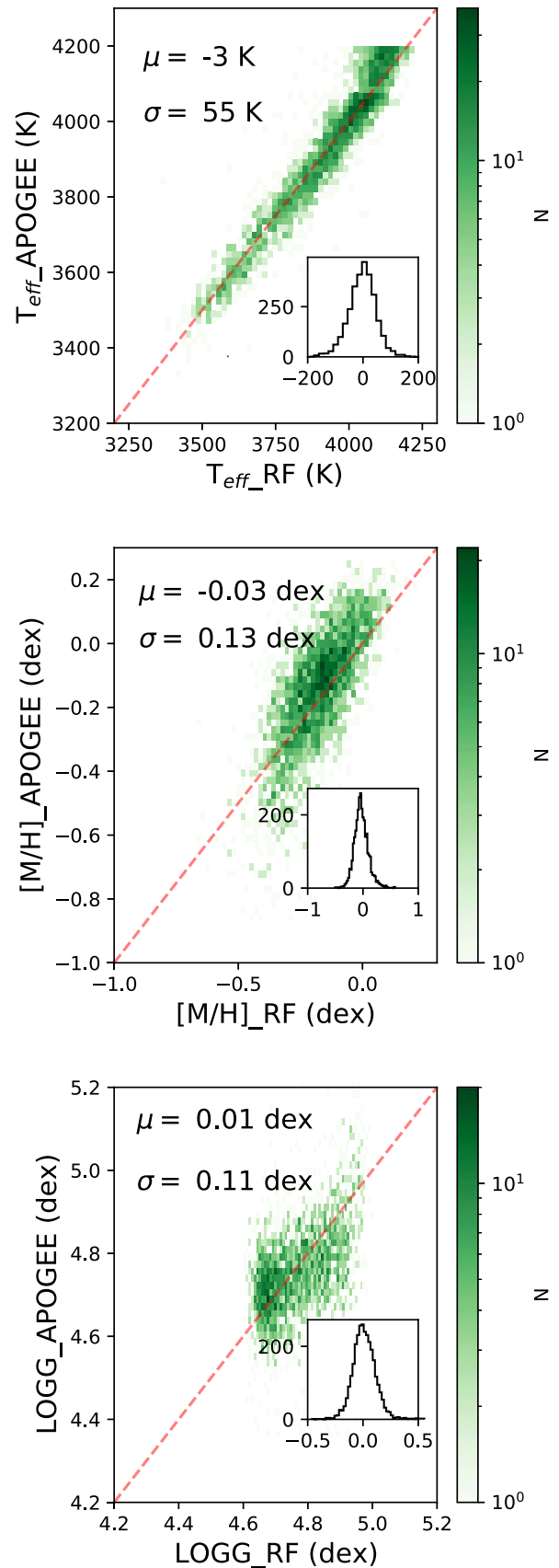


Figure 10. AP comparisons between APOGEE DR16 and the RF values for this work for T_{eff} (top), $[M/H]$ (middle), and $\log g$ (bottom). The difference histogram between this work and APOGEE is plotted inside each panel. The x-axis represents the residual, and the y-axis represents the number of occurrences.

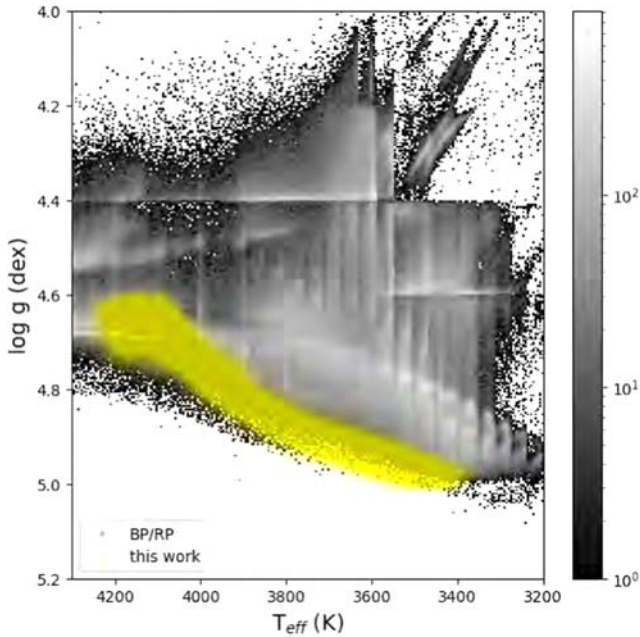


Figure 11. AP comparison between RF values from our work (yellow points) and DR3 APs from BP/RP spectra (gray points) in terms of $\log g$ and T_{eff} .

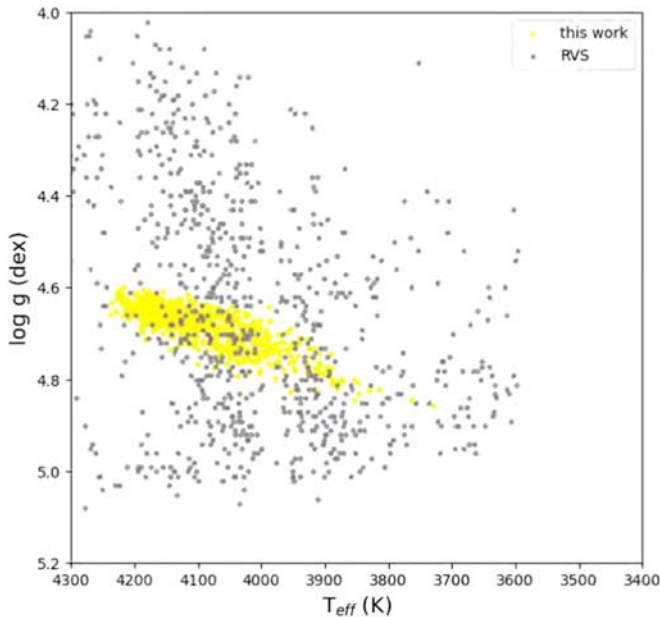


Figure 12. AP comparison of this work with RVS spectra in terms of $\log g$ and T_{eff} . The yellow points represent this work, while the gray points depict RVS spectra.

with 839 objects for comparison. Figure 12 illustrates the AP comparison between RVS and this work. It is immediately obvious from the figure that there are significant discrepancies relative to our expectations based, for example, on the models in Figure 9. The differences here can be attributed to the accuracy of $\log g$ decreasing as T_{eff} decreases (Recio-Blanco et al. 2023).

The σ could be increasing in generating the APs, which is probably caused by two reasons. On the one hand, the ML method prefers to trend the high distribution of the training sample. A bigger scatter would exist if the parameter distribution differed from the training sample. On the other

hand, the APs of cool dwarfs from Gaia need to be used carefully. The limitations cannot be avoided, such as the low resolution of the spectra, the deficiency of the wavelength band, and the lack of a template for cool dwarfs.

5. Summary

In this work, we have developed estimation models for T_{eff} , $[M/H]$, and $\log g$ for cool dwarfs by applying ML methods to optical and infrared photometric data. The main contributions of this paper are summarized as follows.

1. We selected 94,904 objects from the stellar AP catalogs of LAMOST and APOGEE M dwarfs, with T_{eff} ranging from 3200 to 4300 K, $[M/H]$ ranging from -0.1 to 0.5 dex, and $\log g$ larger than 4.5 dex. Using multiband photometry from optical and infrared surveys, two ML methods (RF and LGB) were applied to construct models to predict stellar APs. The parameters showed relative little sensitivity to the chosen ML method and present a best dispersion of 68 K, 0.22 dex, and 0.053 dex for T_{eff} , $[M/H]$, and $\log g$, respectively.
2. We used the SHAP values to analyze the importance of the features during the model building for the APs. According to the SHAP value diagram, it is found that color $W1 - W2$ is the most sensitive feature for both T_{eff} and $\log g$, and that $J - H$ color is most important for $[M/H]$. Infrared photometry plays a crucial role in building our AP models.
3. On the basis of the above work, we have presented a stellar AP catalog of Gaia DR3 cool dwarfs. There are a total of 1,806,921 objects with photometry in eight bands and stellar APs (T_{eff} , $[M/H]$, and $\log g$), as well as their corresponding uncertainties. Comparing our catalog of APs with those from Gaia DR3 BP/RP spectra and RVS suggests a number of issues with the Gaia DR3 APs for cool dwarfs.

Acknowledgments

This work is supported by the National Key R&D Program of China No. 2019YFA0405502, the National Natural Science Foundation of China (12103068, U1931209), a Visiting Fellowship from the Alliance of International Science Organizations, and science research grants from the China Manned Space Project with No. CMS-CSST-2021-B05.

This research has made use of LAMOST data (Luo et al. 2015). The full name of LAMOST is the Large Sky Area Multi-Object Fiber Spectroscopic Telescope or Guoshoujing Telescope. It is a National Major Scientific Project built by the Chinese Academy of Sciences. Funding for the project has been provided by the National Development and Reform Commission. LAMOST is operated and managed by the National Astronomical Observatories, Chinese Academy of Sciences.

This research makes use of data products from Wide-field Infrared Survey Explorer (Wright et al. 2010), which is a joint project of the University of California, Los Angeles, and the Jet Propulsion Laboratory/California Institute of Technology, funded by the National Aeronautics and Space Administration.

This work has made use of data from the European Space Agency (ESA) mission Gaia (<https://cosmos.esa.int/gaia>), processed by the Gaia Data Processing and Analysis

Consortium (DPAC; <https://cosmos.esa.int/web/gaia/dpac/consortium>). Funding for DPAC has been provided by national institutions, in particular the institutions participating in the Gaia Multilateral Agreement.

This work has made use of data products from the Two Micron All Sky Survey (Skrutskie et al. 2006), which is a joint project of the University of Massachusetts and the Infrared Processing and Analysis Center/California Institute of Technology, funded by the National Aeronautics and Space Administration and the National Science Foundation.

This work has made use of data from SDSS DR16 of SDSS-IV (Blanton et al. 2017). Funding for SDSS-IV has been provided by the Alfred P. Sloan Foundation, the Participating Institutions, the National Science Foundation, and the US Department of Energy Office of Science.

This research uses Astropy (<https://www.astropy.org>), TOPCAT (Taylor 2005), Scipy (Virtanen et al. 2020), Numpy (Harris et al. 2020).

ORCID iDs

Cai-Xia Qu  <https://orcid.org/0000-0002-5460-2205>
 A-Li Luo  <https://orcid.org/0000-0001-7865-2648>
 Rui Wang  <https://orcid.org/0000-0001-6767-2395>
 Hugh R. A. Jones  <https://orcid.org/0000-0003-0433-3665>
 Bing Du  <https://orcid.org/0000-0001-6820-6441>
 Xiang-Lei Chen  <https://orcid.org/0000-0001-5738-9625>
 You-Fen Wang  <https://orcid.org/0000-0001-7671-4745>

References

- Almendros-Abad, V., Mužić, K., Moitinho, A., Krone-Martins, A., & Kubiak, K. 2022, *A&A*, 657, A129
- Andrae, R., Fouesneau, M., Sordo, R., et al. 2023, *A&A*, 674, A27
- Bai, Y., Liu, J., Bai, Z., Wang, S., & Fan, D. 2019, *AJ*, 158, 93
- Bessell, M., Bloxham, G., Schmidt, B., et al. 2011, *PASP*, 123, 789
- Blanton, M. R., Bershad, M. A., Abolfathi, B., et al. 2017, *AJ*, 154, 28
- Bochanski, J. J., Munn, J. A., Hawley, S. L., et al. 2007, *AJ*, 134, 2418
- Breiman, L. 1996a, *Mach. Learn.*, 24, 123
- Breiman, L. 1996b, *Ann. Stat.*, 24, 2350
- Bressan, A., Marigo, P., Girardi, L., et al. 2012, *MNRAS*, 427, 127
- Casagrande, L., Flynn, C., & Bessell, M. 2008, *MNRAS*, 389, 585
- Casagrande, L., Lin, J., Rains, A. D., et al. 2021, *MNRAS*, 507, 2684
- Casagrande, L., Silva Aguirre, V., Stello, D., et al. 2014, *ApJ*, 787, 110
- Casagrande, L., & VandenBerg, D. A. 2018a, *MNRAS*, 475, 5023
- Casagrande, L., & VandenBerg, D. A. 2018b, *MNRAS*, 479, L102
- Chen, Y., Bressan, A., Girardi, L., et al. 2015, *MNRAS*, 452, 1068
- Cristofari, P. I., Donati, J. F., Masseron, T., et al. 2022, *MNRAS*, 511, 1893
- Cropper, M., Katz, D., Sartoretti, P., et al. 2018, *A&A*, 616, A5
- Ding, M.-Y., Shi, J.-R., Wu, Y., et al. 2022, *ApJS*, 260, 45
- Du, B., Luo, A. L., Zhang, S., et al. 2021, *RAA*, 21, 202
- Gaia Collaboration, Brown, A. G. A., Vallenari, A., et al. 2016a, *A&A*, 595, A2
- Gaia Collaboration, Creevey, O. L., Sarro, L. M., et al. 2023, *A&A*, 674, A39
- Gaia Collaboration, Prusti, T., de Bruijne, J. H. J., et al. 2016b, *A&A*, 595, A1
- Gaia Collaboration, Vallenari, A., Brown, A. G. A., et al. 2023, *A&A*, 674, A1
- Glass, I. S. 1975, *MNRAS*, 171, 19P
- Green, G. M. 2018, *JOSS*, 3, 695
- Green, G. M., Schlafly, E. F., Finkbeiner, D., et al. 2018, *MNRAS*, 478, 651
- Green, G. M., Schlafly, E. F., Finkbeiner, D. P., et al. 2015, *ApJ*, 810, 25
- Gunn, J. E., Sigmund, W. A., Mannery, E. J., et al. 2006, *AJ*, 131, 2332
- Haqq-Misra, J., Kopparapu, R., Faucher, T. J., et al. 2022, *PSJ*, 3, 60
- Harris, C. R., Millman, K. J., van der Walt, S. J., et al. 2020, *Natur*, 585, 357
- Holtzman, J. A., Hasselquist, S., Shetrone, M., et al. 2018, *AJ*, 156, 125
- Hu, Z., Chen, J., Jiang, B., & Wang, W. 2021, *Univ*, 7, 438
- Jones, H. R. A., Longmore, A. J., Allard, F., & Hauschildt, P. H. 1996, *MNRAS*, 280, 77
- Kaiser, N., Aassel, H., Burke, B. E., et al. 2002, *Proc. SPIE*, 4836, 154
- Ke, G., Meng, Q., Finley, T., et al. 2017, Advances in Neural Information Processing Systems 30, ed. I. Guyon et al. (NeurIPS), 3146, https://papers.nips.cc/paper_files/paper/2017/hash/6449f44a102fde848669bdd9eb6b76fa-Abstract.html
- Lépine, S., Rich, R. M., & Shara, M. M. 2003, *AJ*, 125, 1598
- Li, J., Liu, C., Zhang, B., et al. 2021, *ApJS*, 253, 45
- Liang, J., Bu, Y., Tan, K., et al. 2022, *AJ*, 163, 153
- Lin, J., Casagrande, L., & Asplund, M. 2022, *MNRAS*, 510, 433
- Lundberg, S. M., & Lee, S.-I. 2017, Advances in Neural Information Processing Systems 30, ed. I. Guyon et al. (NeurIPS), 4765, https://papers.nips.cc/paper_files/paper/2017/hash/8a20a8621978632d76c43dfd28b67767-Abstract.html
- Luo, A. L., Zhao, Y.-H., Zhao, G., et al. 2015, *RAA*, 15, 1095
- Malik, A., Moster, B. P., & Obermeier, C. 2022, *MNRAS*, 513, 5505
- Neugebauer, G., & Leighton, R. B. 1969, Two-micron Sky Survey. A Preliminary Catalogue (Washington, DC: NASA)
- Passegger, V. M., Wende-von Berg, S., & Reiners, A. 2016, *A&A*, 587, A19
- Planck Collaboration, Abergel, A., Ade, P. A. R., et al. 2014, *A&A*, 571, A11
- Rajpurohit, A. S., Allard, F., Rajpurohit, S., et al. 2018, *A&A*, 620, A180
- Rayner, J. T., Toomey, D. W., Onaka, P. M., et al. 2003, *PASP*, 115, 362
- Recio-Blanco, A., de Laverny, P., Palicio, P. A., et al. 2023, *A&A*, 674, A29
- Ribeiro, F., & Gradwohl, A. L. S. 2021, *A&C*, 35, 100468
- Rojas-Ayala, B., Covey, K. R., Muirhead, P. S., & Lloyd, J. P. 2010, *ApJL*, 720, L113
- Rojas-Ayala, B., Covey, K. R., Muirhead, P. S., & Lloyd, J. P. 2012, *ApJ*, 748, 93
- Sarro, L. M., Berihuete, A., Smart, R. L., et al. 2023, *A&A*, 669, A139
- Schmidt, S. J., Wagoner, E. L., Johnson, J. A., et al. 2016, *MNRAS*, 460, 2611
- Skrutskie, M. F., Cutri, R. M., Stiening, R., et al. 2006, *AJ*, 131, 1163
- Taylor, M. B. 2005, in ASP Conf. Ser. 347, Astronomical Data Analysis Software and Systems XIV, ed. P. Shopbell, M. Britton, & R. Ebert (San Francisco, CA: ASP), 29
- Virtanen, P., Gommers, R., Oliphant, T. E., et al. 2020, *NatMe*, 17, 261
- Wright, E. L., Eisenhardt, P. R. M., Mainzer, A. K., et al. 2010, *AJ*, 140, 1868
- Yang, L., Yuan, H., Xiang, M., et al. 2022, *A&A*, 659, A181
- York, D. G., Adelman, J., Anderson, J. E. J., et al. 2000, *AJ*, 120, 1579
- Yuan, H. B., Liu, X. W., & Xiang, M. S. 2013, *MNRAS*, 430, 2188
- Zhang, B., Liu, C., & Deng, L.-C. 2020, *ApJS*, 246, 9
- Zhang, X., Green, G. M., & Rix, H.-W. 2023, *MNRAS*, 524, 1855
- Zheng, J., Zhao, G., Wang, W., et al. 2018, *RAA*, 18, 147